OCEANOGRAPHY

Ocean eddies strongly affect global mean sea-level projections

René M. van Westen* and Henk A. Dijkstra

Current sea-level projections are based on climate models in which the effects of ocean eddies are parameterized. Here, we investigate the effect of ocean eddies on global mean sea-level rise (GMSLR) projections, using climate model simulations. Explicitly resolving ocean eddies leads to a more realistic Southern Ocean temperature distribution and volume transport. These quantities control the rate of basal melt, which eventually results in Antarctic mass loss. In a model with resolved ocean eddies, the Southern Ocean temperature changes lead to a smaller Antarctic GMSLR contribution compared to the same model in which eddies are parameterized. As a result, the projected GMSLR is about 25% lower at the end of this century in the eddying model. Relatively small-scale ocean eddies can hence have profound large-scale effects and consequently affect GMSLR projections.

INTRODUCTION

Satellite-observed sea-level measurements indicate an ongoing increase in the global mean sea level since the satellite era (*1*–*3*). Global mean sea-level rise (GMSLR) threatens low-lying coastal regions, and these regions will benefit strongly from sea-level projections to adapt their coastal protection infrastructure (*4*, *5*). Useful scenarios of future global mean sea-level change in the upcoming decades can only be made by state-of-the-art climate models. Current projections are based on climate models in which ocean-eddy processes are parameterized and the present-day state in these models strongly deviates from available observations, in particular, in the Southern Ocean (*6*, *7*).

The climate models used in the fifth Intergovernmental Panel on Climate Change Assessment Report provide estimations of GMSLR in the upcoming decades (*6*). One of the greatest uncertainties at that time was the contribution by the Antarctic ice sheet (AIS) to GMSLR (*8*), and it was noted that marine ice-sheet instability of the West Antarctic ice sheet could change the GMSLR projections by several decimeters (*9*, *10*). Since then, observational studies have shown that the Antarctic contribution to GMSLR is increasing over time, in particular, for western Antarctica due to basal melt near the grounding line of various ice shelfs and glaciers (*1*, *11*, *12*).

In a recent model study (*7*), 16 state-of-the-art AIS models subject to basal melt were used to determine the sea-level response by ice loss. Basal melt of ice shelfs was driven by subsurface ocean temperatures obtained from global climate model simulations within the Coupled Model Intercomparison Project phase 5 (CMIP5). However, the present-day state of the Southern Ocean and its responses to climate change strongly differ among the CMIP5 models (*13*, *14*); this holds as well for the older CMIP phase 4 models (*15*, *16*). Differences (e.g., temperature and salinity) in the mean state, compared to the available observations, have been attributed to the coarse horizontal (ocean model) resolution in these models (*17*–*19*).

In ocean models with a higher spatial resolution, where eddies are partly represented, the present-day Southern Ocean surface temperature is much better represented compared to that in ocean models where eddies are parameterized (*20*). Explicitly representing eddies in one climate model also leads to substantially different regional dynamic sea-level projections for the Caribbean compared to version of the same model where eddies are parameterized (*21*). Motivated by these results, we here analyze GMSLR projections in two (noneddying and eddying) versions of the Community Earth System Model (CESM), taking into account Antarctic basal melt under a particular climate change scenario.

RESULTS

Climate model simulations

The CESM is a fully coupled state-of-the-art global climate model and is participating in the CMIP5 and CMIP6 efforts. The high-resolution version of CESM (HR-CESM) used here has an ocean component with a 10-km (0.1°) horizontal resolution, capable of capturing the development and interaction of mesoscale ocean eddies (*22*), and an atmosphere component with a horizontal resolution of 50 km (0.5°). Both the ocean and atmosphere component of the low-resolution version of the CESM (LR-CESM) have a horizontal resolution of 100 km (1°). The ocean component of this low-resolution model cannot generate mesoscale ocean eddies. The high-resolution and the low-resolution versions of the CESM are spun up by 200 and 500 years, respectively, under a present-day (year 2000) forcing and then continued for 101 years under the same forcing to give the 101-year HR-CESM control and LR-CESM control simulations. The HR-CESM and LR-CESM simulations are initiated from the end of the corresponding spin up and are forced under a 1% pCO_2 increase each year (model years 2000–2100). More details of the CESM simulations can be found in Materials and Methods. Both CESM versions have a volume conservation constraint for the ocean component and do not capture dynamical ice sheets. The contributions of the mass loss of glaciers and ice sheets to the GMSLR therefore need to be determined by post-processing of the model results (see Materials and Methods). The CESM does not include any changes in the land-water storage.

Since observations of the Southern Ocean are limited, we compare the CESM control simulations results with one reanalysis product, the Mercator data, in which available observations are assimilated. Figure S1 (A, C, and D) shows the time mean (26 years) and depth-averaged (250 to 450 m) oceanic temperature fields for Mercator, HR-CESM control, and LR-CESM control, respectively. The depth range is based on the mean depth of the various

Institute for Marine and Atmospheric Research, Utrecht University, Princetonplein 5, 3584 CC Utrecht, Netherlands.
*Corresponding author. Email: r.m.vanwesten@uu.nl

Antarctic ice shelfs (*7*). The HR-CESM control is much better in agreement with reanalysis compared to the LR-CESM control. For example, the area-weighted correlation pattern [root mean square (RMS) deviation] over the 80°S to 60°S band is about 10% higher (45% lower) for the HR-CESM control compared to the LR-CESM control and is robust over the simulation period (fig. S1B). For the HR-CESM control, the largest temperature difference with respect from Mercator is found west of the Antarctic Peninsula with a magnitude of about −2°C (fig. S1E). The LR-CESM control is warmer compared to Mercator in the Weddell Gyre and along the (eastern) Antarctic continental shelf (fig. S1F). The results in fig. S1 indicate that ocean subsurface temperature differences (with respect to Mercator) are reduced under a higher spatial resolution of the ocean model.

The RMS deviation is increasing over time, indicating that there is a slight drift in the control simulations (figs. S1B and S2, A and B). For the LR-CESM control, the temperature trends are persistent over the analyzed period. On the contrary, in the HR-CESM control, part of these (significant) trends is related to multidecadal variability in the Southern Ocean (*23*). This multidecadal variability is related to ocean-eddy interactions with the background flow (*24*), which are absent in the LR-CESM control.

Global mean sea-level rise

The GMSLR in the HR-CESM and LR-CESM simulations consists of four contributions, and these are shown over the 101-year period in Fig. 1 (A and B); details on the computation of each contribution can be found in Materials and Methods. The largest contribution to GMSLR is caused by (thermo)steric effects (adjusted for drift in each control simulation). The second largest and third (largest) contributions are related to melt by glaciers (fig. S3) and changes in the surface mass balance of the Greenland ice sheet (GrIS; fig. S4), respectively. These three contributions to GMSLR are fairly similar for both HR-CESM and LR-CESM (Fig. 1, A and B). The fourth contribution to GMSLR is due to changes in the surface mass balance and mass loss as a result of basal melt of the AIS (fig. S5). The Antarctic contribution strongly differs between the HR-CESM and the LR-CESM, where the LR-CESM projected value for Antarctica in the year 2100 is 9.3 cm higher compared to that of the HR-CESM. Note that the mass loss by basal melt is balanced by changes in surface mass balance in the HR-CESM (fig. S5A), resulting in a near-zero contribution for the AIS.

The patterns of sea-level change between two 30-year periods (2071–2100 and 2000–2029) are shown for HR-CESM and LR-CESM in Fig. 1 (C and D), respectively. Here, gravitational, rotational, and deformation [GRD; (*25*)] effects by mass loss of glaciers and ice sheets are taken into account (see also figs. S3 to S5). Ocean currents change under global warming, affecting the dynamic sea level. The largest dynamic sea-level changes over time are found in the Southern Ocean and near western boundary currents for both HR-CESM and LR-CESM (fig. S6). Dynamic sea-level changes are also included in the local sea-level rise (Fig. 1, C and D) but do not contribute to GMSLR since the ocean has a volume conservation constraint.

The local sea level is projected to rise over the 2000–2100 period for most of the ocean surface in both simulations (Fig. 1, C and D). In the south of Greenland, the sea-level rise displays a dipole pattern

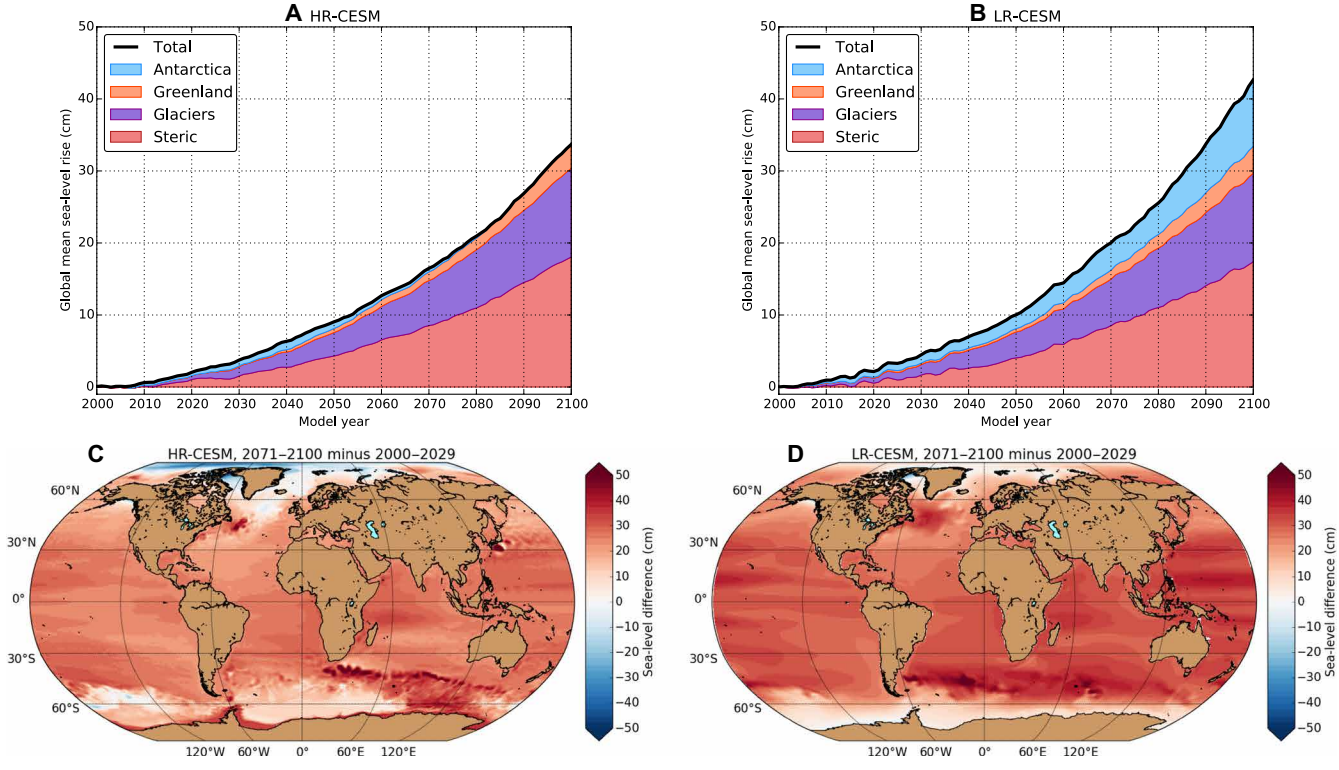

Fig. 1. Contributions to GMSLR. (**A** and **B**) Contributions to global mean sea-level rise over the 101-year period for the HR-CESM and LR-CESM, respectively; the black curve indicates the total global mean sea-level rise. (**C** and **D**) The local sea-level difference between the time mean over years 2071–2100 and time mean over years 2000–2029 for the HR-CESM and LR-CESM, respectively.

of relatively higher and lower sea-level rise compared to the surroundings. This is associated with a weaker Atlantic meridional overturning circulation in both simulations (*21*), consistent with currently available observations (*26*, *27*). The sea-level changes in the Southern Ocean are mostly caused by dynamic sea-level changes (fig. S6); however, these patterns differ substantially between the HR-CESM and LR-CESM. For example, there is a notable difference in the South Atlantic and Weddell Sea regions partly caused by the effects of ocean eddies on the path of the Agulhas Current (*28*). Agulhas Current changes (causing dynamic sea-level changes) contribute up to 60% of the local sea-level rise for the HR-CESM, and this is only up to 25% in the same region for the LR-CESM.

Antarctic basal melt

To further analyze the differences in Antarctic basal melt between LR-CESM and HR-CESM, we follow the procedure outlined in

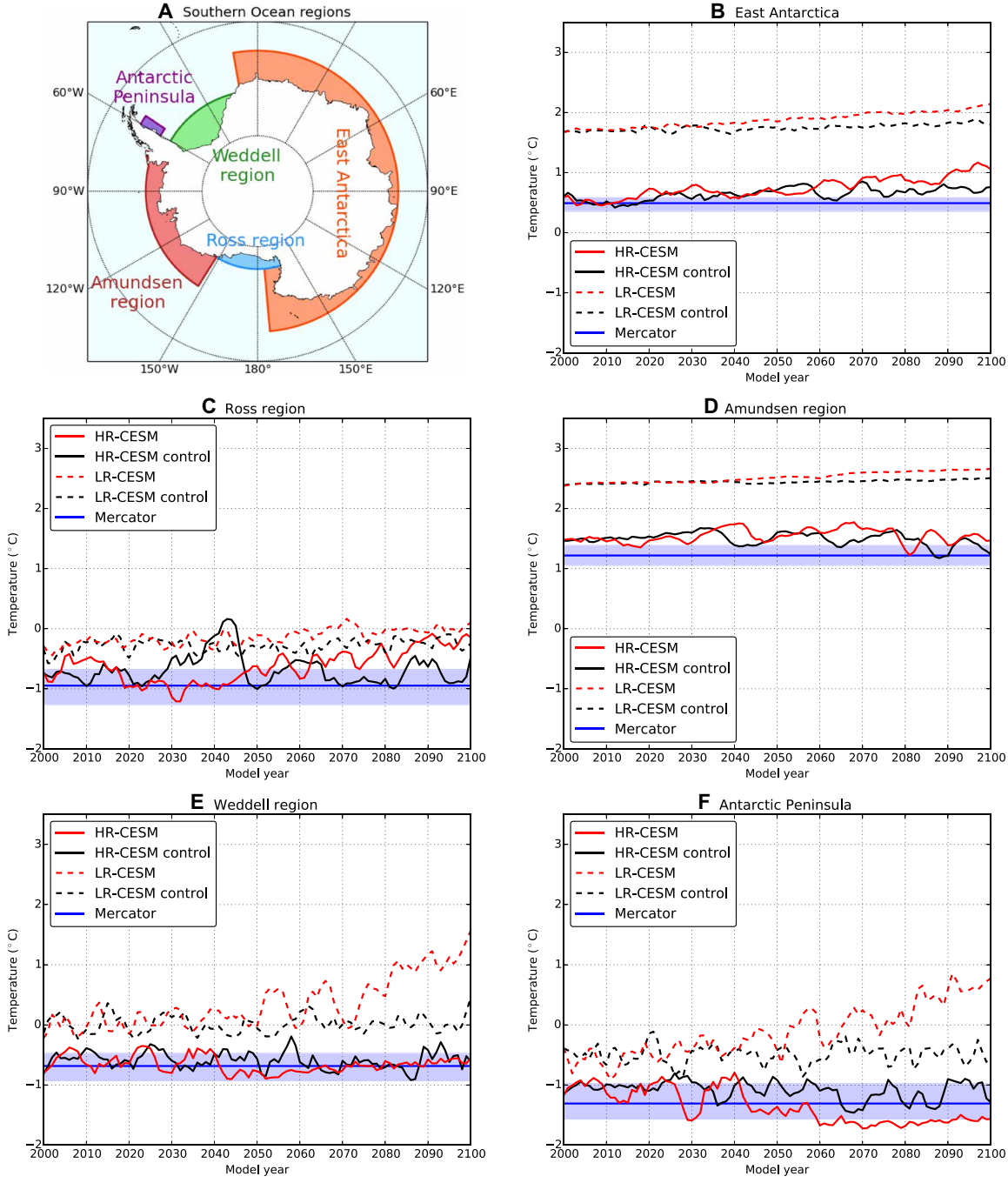

Fig. 2. Southern Ocean regions and temperatures in the CESM. (**A**) The five Southern Ocean regions over which the basal melt is determined, similar to those in Levermann *et al.* (*7*). (**B** to **F**) Time evolution of the regional and depth-averaged oceanic temperature of the five Southern Ocean regions for the CESM simulations. For Mercator, the time mean over 1993–2018 is displayed (solid lines) and the shading indicates the minimum and maximum temperature over this period.

Table 1. Overview of the CESM and CMIP6 models and the spatial resolution of their ocean component lon, longitude; lat, latitude.

Model	lon × lat	Nominal resolution	Vertical layers
	(number of grid cells)	(km)	
HR-CESM	3600 × 2400	10	42
LR-CESM	320 × 384	100	60
ACCESS-CM2	360 × 300	100	50
ACCESS-ESM1-5	360 × 300	100	50
AWI-CM-1-1-MR	Unstructured	25	46
BCC-CSM2-MR	360 × 232	100	40
BCC-ESM1	360 × 232	100	40
CAMS-CSM1-0	360 × 200	100	50
CanESM5	360 × 291	100	45
CanESM5-CanOE	360 × 291	100	45
CESM2	320 × 384	100	60
CESM2-FV2	320 × 384	100	60
CESM2-WACCM	320 × 384	100	60
CMCC-CM2-SR5	362 × 292	100	50
CNRM-CM6-1	362 × 294	100	75
CNRM-CM6-1-HR	1442 × 1050	25	75
CNRM-ESM2-1	362 × 294	100	75
EC-Earth3-Veg	362 × 294	100	75
GFDL-CM4	1440 × 1080	25	35
GFDL-ESM4	720 × 576	50	35
GISS-E2-1-G	288 × 180	250	40
HadGEM3-GC31-LL	360 × 330	100	75
IPSL-CM6A-LR	362 × 332	100	75
MIROC-ES2L	360 × 256	100	63
MIROC6	360 × 256	100	63
MPI-ESM1-2-HAM	256 × 220	250	70
MPI-ESM1-2-HR	802 × 404	50	70
MPI-ESM1-2-LR	256 × 220	250	70
NorCPM1	320 × 384	100	35
NorESM2-LM	360 × 385	100	70 [ρ(*z*) coordinates]
NorESM2-MM	360 × 385	100	70 [ρ(*z*) coordinates]
SAM0-UNICON	320 × 384	100	60
UKESM1-0-LL	360 × 330	100	75

Levermann *et al.* (*7*) (see Materials and Methods). Positive oceanic temperature anomalies drive the basal melt of the ice sheets, which are shown here using five different regions in the Southern Ocean (Fig. 2A). For each region, we determined the vertically averaged subsurface temperature over a range of 100 m [for the specific depth ranges of the region, see table 1 in Levermann *et al.* (*7*)]. The time series for the five regions are shown in Fig. 2 (B to F) for the CESM simulations; also, the Mercator time mean and variability between 1993 and 2018 is plotted. The HR-CESM control reasonably matches with Mercator for the five different regions. On the contrary, the LR-CESM control is about 0.5° to 1.5°C warmer compared to Mercator for the five different regions.

In the second half of the simulation, the LR-CESM temperature starts to deviate from the LR-CESM control temperature. In all regions (Fig. 2, B to F), a warming occurs over time (see also fig. S2D). Significant and positive (lag-)correlations are therefore found between the 2-m global mean surface temperature (GMST) anomaly and the five Southern Ocean regions for the LR-CESM (fig. S7), similar to the ones in Levermann *et al.* (*7*). The temperature anomalies are deviations from the respective control simulation (so not with respect to Mercator) and are adjusted for any drift (see Materials and Methods). For the HR-CESM, only East Antarctica and the Ross region (Fig. 2, B and C, and fig. S2C) are deviating from the HR-CESM control and for these two regions, significant (lag-) correlations exist with the GMST anomaly (fig. S7, A and B). There are no positive temperature anomalies (apart from natural variability) for the other three regions over the 101-year period for the HR-CESM and, hence, the lag-correlations with the GMST anomaly for these three regions are much smaller than those in the LR-CESM (fig. S7, C to E). The Southern Ocean subsurface temperature anomalies at the end of the century are positive for the LR-CESM and the largest anomalies are found in the southwestern part of the Weddell Sea (fig. S2D). On the contrary, the HR-CESM displays both positive and negative temperature anomalies in the Southern Ocean (fig. S2C). A nearly linear (positive) dependence of the GMST anomaly on the Southern Ocean temperature anomalies, a typical CMIP5 response (*7*), does not hold for the HR-CESM.

Most models participating in CMIP6 (see Materials and Methods) have the same horizontal ocean model resolution as the LR-CESM (i. e. ,1°, see Table 1). There is a large variety in temperatures of the five Southern Ocean Regions for the CMIP6 ensemble, in particular, for the GMST, Ross region, and Amundsen region (fig. S8). Note that the CMIP6 control simulations cannot directly be compared to our CESM simulations because they have a preindustrial forcing. However, the temperature response of the CMIP6 simulations under the 1% CO_2 increase scenario can be compared. The CMIP6 subsurface temperature anomalies (with respect to control simulations) of the last 30 years are shown in fig. S9 and are similar to the ones in fig. S2 (C and D). There is a large variety of temperature responses among the CMIP6 models, and the largest differences between the CMIP6 models are found near the Antarctic continental shelfs. The CMIP6 model mean has a positive temperature response over the whole Southern Ocean. The HR-CESM temperature anomaly pattern (fig. S2C) is most closely correlated with that of the GFDL-CM4 and CNRM-CM6-1-HR patterns, with a spatial correlation pattern value of r = 0.40 (Fig. 3A). The GFDL-CM4 and CNRM-CM6-1-HR have one of the highest horizontal ocean resolution (25 km) of the suite of CMIP6 models and are ocean-eddy permitting. Low correlation pattern values ($|r| < 0.3$) are found between the HR-CESM and most CMIP6 models and including the LR-CESM (Fig. 3A). The LR-CESM temperature pattern (fig. S2D) has great similarities with that of the CMIP6 CESM models (CESM2, CESM2-FV2, and CESM2-WACCM), and relatively high correlation pattern values (r = 0.64 to 0.72) are found between the LR-CESM and CMIP6 CESM models (Fig. 3B).

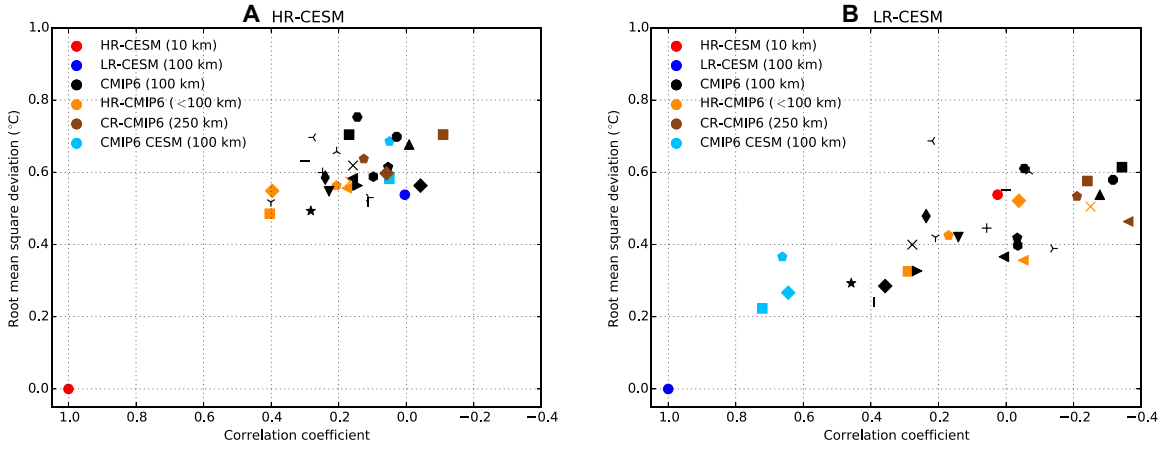

Fig. 3. Southern Ocean temperature comparison with CMIP6. (**A**) The area-weighted correlation pattern and RMS deviation between the HR-CESM temperature anomalies (fig. S2C) and those of the 31 CMIP6 models (fig. S9), as well as the LR-CESM (fig. S2D), between 80°S and 60°S. Before determining the correlation and RMS deviation, the HR-CESM pattern is interpolated onto each of the CMIP6 models native grid and the LR-CESM grid. (**B**) Similar to (A), but now, the LR-CESM is interpolated onto the CMIP6 models native grid and the HR-CESM grid. The CMIP6 models are categorized in four groups: the higher-resolution CMIP6 models (HR-CMIP6, nominal ocean model horizontal resolution < 100 km), the coarse-resolution CMIP6 models (CR-CMIP6, nominal resolution of 250 km), the CMIP6 CESM models (nominal resolution of 100 km), and the remaining CMIP6 models (nominal resolution of 100 km). Markers indicate the different models within each category.

The GMST is increasing for all CMIP6 models and the HR-CESM and LR-CESM responses are fairly similar to most of the CMIP6 models (fig. S10A). For East Antarctica (fig. S10B) and the Ross region (fig. S10C), the CESM simulations have a similar response to the CMIP6 models, but the anomalies are mainly below the CMIP6 mean. The HR-CESM hardly shows any positive temperature anomalies and is below the CMIP6 model mean for the Amundsen region (fig. S10D), Weddell region (fig. S10E), and the Antarctic Peninsula (fig. S10F). On the contrary, the LR-CESM is warming for these three regions, in particular, for the Weddell region and Antarctic Peninsula during the last 30 years of the simulation. The model mean of the five higher-resolution CMIP6 models (HR-CMIP6) tends to stay below the CMIP6 mean for the Amundsen region, Weddell region, and Antarctic Peninsula, similar to the HR-CESM. For the other two regions, the HR-CMIP6 remains close to the CMIP6 mean.

The temperature anomalies are converted to GMSLR equivalent by using response functions from ice-sheet models, which are subject to basal melt (*7*). The largest GMSLR as a result of basal melt from the five Southern Ocean regions is the Weddell region and this region also displays the largest spread among the CMIP6 models (Fig. 4). For each region, the GMSLR as a result of basal melt for the HR-CESM and LR-CESM is within the CMIP6 ensemble. However, the HR-CESM is below the CMIP6 mean for each region, which results in a total GMSLR contribution outside the CMIP6 ensemble band at the end of the simulation.

The contribution as a result of basal melt to GMSLR (fig. S5, A and B, red curve) is partly compensated by an increase in snowfall over the AIS (fig. S5, A and B, blue curve). For the HR-CESM (LR-CESM), the AISs warm by a factor of 1.1 (1.3) with respect to the GMST anomaly and snowfall increases at 6.6%°C^{-1} (6.2 %°C^{-1}) by Antarctic warming. These rates over the AISs are similar to the ones reported in the literature (*29*) (e.g., 1.1 ± 0.2 and 5.1 ± 1.5%°C^{-1}).

Recent observations (*12*) indicate that West Antarctica contributes 7.3 mm (55% of total AIS) to GMSLR between 1979 and 2017. Of this 7.3 mm, 6 mm (80%) originates from the Pine Island, Thwaites, and Crosson glaciers. These three glaciers are situated in the Amundsen region. For the HR-CESM and LR-CESM simulations (Fig. 4D), the GMSLR contribution of the Amundsen region is 5.3 and 4.4 mm in 101 years, respectively, which is considerably less compared to observations. In addition, the GMSLR contribution at the end of the simulation from the Weddell region is a factor 1.5, 18, and 3.4 higher compared to that of the Amundsen region for the HR-CESM, LR-CESM, and CMIP6 model mean, respectively. This demonstrates that either the GMSLR contribution by the Amundsen region is underestimated and/or that the GMSLR contribution by the Weddell region is overestimated by the different models.

The discrepancy between observations and models can be explained as follows. The temperature anomaly of the Amundsen region is not always representative for the temperature anomaly near the ice shelves where the basal melt occurs. The time-mean (model years 2071–2100) temperature anomaly of the Amundsen region is 0.08°C and 0.15°C for the HR-CESM and LR-CESM, respectively (fig. S10D). Over the same period, there are both positive (up to 1.1°C) and negative (down to −1.0°C) temperature anomalies in the Amundsen region for the HR-CESM (fig. S2C). For the LR-CESM, the temperature anomaly pattern in the Amundsen region is more homogeneous, and we find only positive temperature anomalies varying between 0.09°C and 0.34°C (fig. S2D).

In the ideal case, one would like to consider the subsurface temperature anomaly for each individual glaciers (e.g., the Pine Island, Thwaites, and Crosson glaciers). However, to resolve the ocean circulation near ice shelves, an even higher horizontal resolution is required [i.e., 200 m; (*30*)], which is about a factor 15 higher compared to that of the HR-CESM. Even if the temperature anomalies of each glacier is known, the corresponding response function is required and these are not available.

The relatively large GMSLR contribution of the Weddell region in the LR-CESM is due to model deficiencies (Fig. 3B). In all the low-resolution CESM simulations, strong positive temperature anomalies occur near the Weddell region (compare fig. S2D with

fig. S9). These positive temperature anomalies in the Weddell region disappear in the HR-CESM (Fig. 3A).

Changes in the Southern Ocean circulation

To understand the difference between the temperature responses of HR-CESM and LR-CESM for the Weddell region and Antarctic Peninsula, the barotropic streamfunction (BSF), which measures changes in the vertically averaged circulation in the Southern Ocean, see Materials and Methods, is analyzed. The time-mean BSF fields (model years 2000–2029) of both simulations are shown in Fig. 5 (A and B). The large-scale pattern of the Antarctic circumpolar current (ACC) is represented in both simulations, as well as the Weddell Gyre and the Ross Gyre. The observed volume transport through Drake Passage is about 135 ± 10 sverdrup (Sv) (*31*, *32*) (1 Sv ≡ 10^6 m^3 s^{-1}), while the modeled volume transport for the HR-CESM control with a time mean of 133 Sv (126 to 141 Sv, 101 years) is close to observations. The LR-CESM control has a much larger volume transport compared to observations with a time-mean value

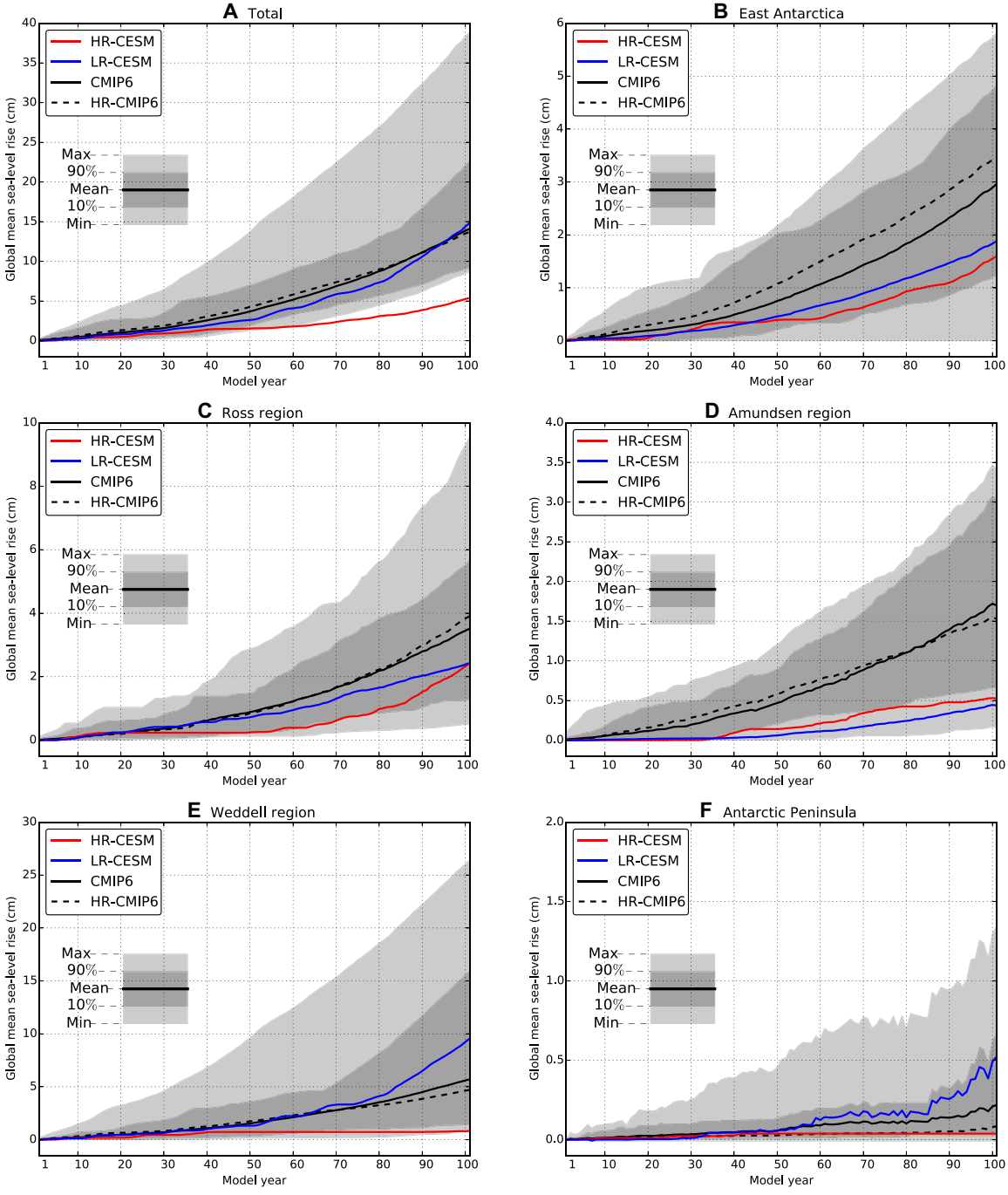

Fig. 4. GMSLR as a result of basal melt. (**A**) Global mean sea-level rise as a result of basal melt of the AIS for the HR-CESM, LR-CESM, and CMIP6 models. (**B** to **F**) Global mean sea-level rise contribution from each of the five Southern Ocean regions (cf. Fig. 2A). Note that the vertical axes have different ranges.

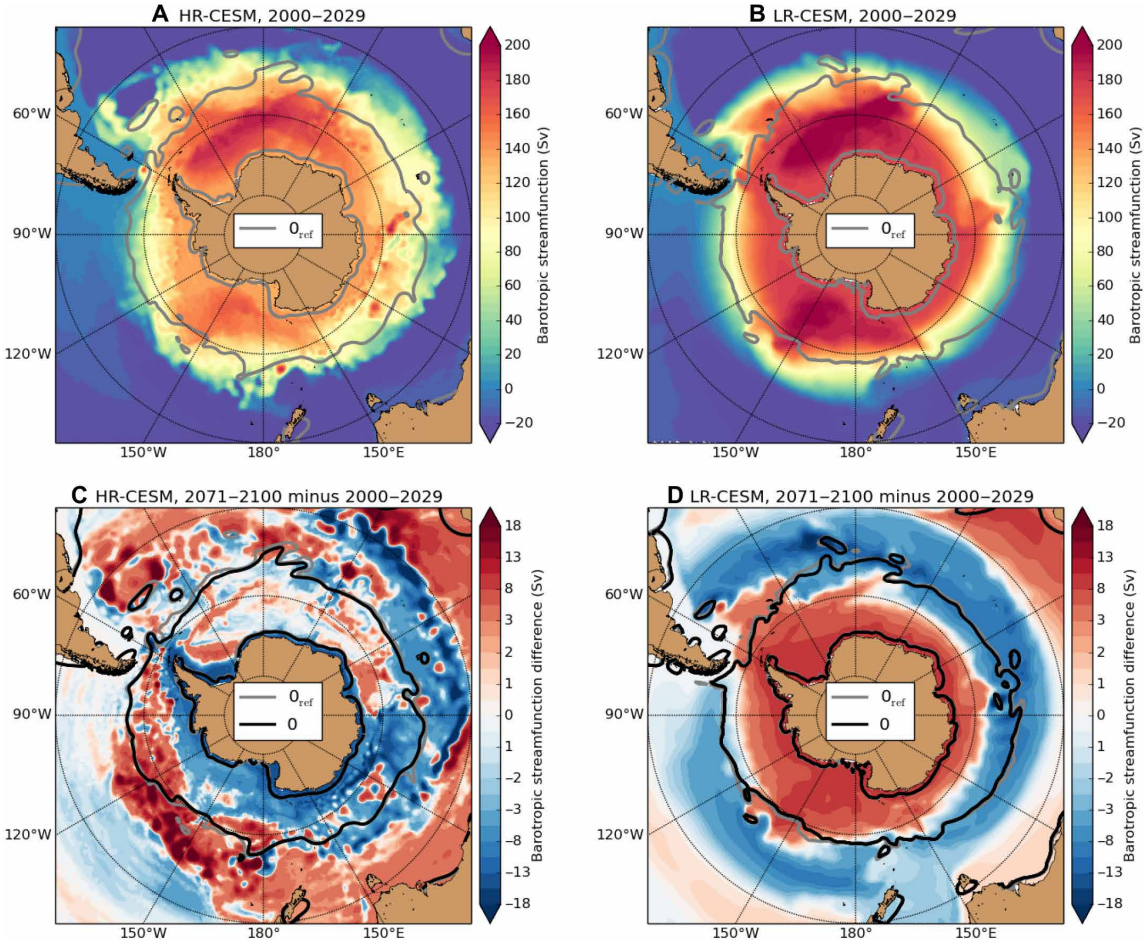

Fig. 5. Changes in BSF and wind-stress curl in the Southern Ocean. (**A** and **B**) Time mean over years 2000–2029 of the barotropic streamfunction (BSF) for the HR-CESM and LR-CESM. (**C** and **D**) Difference in BSF for the HR-CESM and LR-CESM between the time mean over years 2071–2100 and time mean over years 2000–2029. The gray and black contours show the zero wind-stress curl over (A and B) years 2000–2029 and (C and D) years 2071–2100, respectively (so not the difference over both periods), where 0_{ref} indicates the time-mean over years 2000–2029. The wind-stress curl fields for the HR-CESM are smoothed by a Gaussian filter.

of 160 Sv (152 to 164 Sv, 101 years). It is well known that ocean eddies strongly affect the momentum balances in the Southern Ocean (*33*) determining the ACC strength.

The difference between the time-mean BSF fields over the years 2071–2100 and the years 2000–2029 is shown in Fig. 5 (C and D) for both HR-CESM and LR-CESM, respectively. The LR-CESM displays an increase in the BSF values between latitudes of 80°S to 60°S and decreasing BSF values between latitudes of 60°S to 40°S, increasing the meridional BSF gradient and consequently increasing the ACC strength. For the HR-CESM, the increase in the meridional BSF gradient between these latitudes bands is small. However, there is an increase (more negative) in the meridional BSF gradient close to the Antarctic continent for the HR-CESM, which leads to an increase in the Antarctic Coastal Current (fig. S11, A and C). This current is poorly resolved (fig. S11) in the LR-CESM. The total westward volume transport of the Antarctic Coastal Current (near the Weddell Gyre) in the HR-CESM increases by about 10 Sv (compared to the HR-CESM control) in the last 20 years of the simulation (fig. S11E). This increase in westward transport is related to an intensification of the Weddell Gyre. The wind-stress curl is similar for the HR-CESM between the earlier and later period of the simulation (Fig. 5) and hence is not responsible for this intensification.

The modeled Antarctic sea-ice extent in the HR-CESM control and LR-CESM control reasonably matches with that of observations (1993–2018; see Materials and Methods) but is lower compared to observations (fig. S12, A and B). For example, in the HR-CESM control, LR-CESM control, and observations, the annual maximum sea-ice extent is ranging between 14.8 million and 18.3 million km^2 (101 years), 13.9 million and 15.7 million km^2 (101 years), and 18.6 million and 20.9 million km^2 (26 years), respectively. In the HR-CESM, the sea ice is rapidly decreasing in the last 30 years of the simulation, especially in the Weddell Sea (fig. S12, A, C, and E). Less Antarctic sea ice results in more vorticity input by the wind and, from this, an intensification of the Weddell Gyre. The temporal intensification of the Weddell Gyre in the HR-CESM control (fig. S11E) is associated with Maud Rise polynya and Weddell polynya formation. These Maud Rise polynyas also form in the HR-CESM (around 3°E, 65°S in fig. S12C). There is no substantial sea-ice loss in the Weddell Sea and no polynya formation (*23*) for the LR-CESM (fig. S12, B, D, and F) and, hence, the Weddell Gyre strength does not increase (fig. S11, B, D, and F).

An increase in the Weddell Gyre strength will thermally isolate the Weddell region and the Antarctic Peninsula, similar to the ACC thermally isolating Antarctica from the lower latitude Southern Ocean. This explains the absence of subsurface warming for these two regions in the HR-CESM. For the LR-CESM, only the large-scale ocean circulation (i.e., ACC) is affected under climate change, but not the Weddell Gyre and Antarctic Coastal Current. Relatively, warm water from the Weddell Gyre is in this model advected toward the Weddell region and Antarctic Peninsula, leading to relatively large temperature changes there.

DISCUSSION

For the two different versions of the CESM (HR-CESM and LR-CESM), the overall responses to the increase in CO_2 [GMST, contributions by glaciers to the GMSLR (*34*), thermo(steric) effects (*21*), and surface mass balance changes of the GrIS (*35*)] are quite similar and compare also well to 31 CMIP6 models analyzed. The projected temperature change and snowfall anomaly over the AIS for the HR-CESM and LR-CESM are also similar to the ones reported in Gregory and Huybrechts (*29*).

However, the Antarctic basal melt (*7*) strongly deviates between the HR-CESM and LR-CESM. The HR-CESM and LR-CESM simulations provide GMSLR projections of 5.4 ± 0.3 cm (95% confidence level) and 15 ± 0.8 cm (95% confidence level) through basal melt in 2100, respectively, which gives a factor 2.8 difference. The LR-CESM GMSLR projection of basal melt is within CMIP6 projections, but the HR-CESM projects quite lower GMSLR values with respect to CMIP6 ones. These differences in basal melt are related to the different horizontal resolutions in the ocean component of the models.

The Southern Ocean is a rather complex region where the large-scale ocean circulation, mesoscale ocean eddies, sea-ice formation, and atmospheric processes all play an important role in the response under global warming. Mesoscale ocean eddies are highly relevant for the redistribution and transport of heat and salt (*20*, *22*, *36*, *37*) and are critical for the correct momentum balance for the large-scale circulation. Explicitly resolving ocean eddies in the HR-CESM does not only lead to a better representation of the present-day subsurface temperature distribution surrounding Antarctica (compared to LR-CESM) but also to a different response under global warming. For the HR-CESM, we find changes on both the large scale (e.g., in the ACC, sea-ice fields) and the regional scale (Weddell and Ross gyres and the Antarctic Coastal Current), while in the LR-CESM (and CMIP6 models), these occur only on the large scale.

Because of the extreme computational costs, there is unfortunately only one high-resolution simulation available for the analysis done here (HR-CESM control and HR-CESM). More of those simulations are required to provide a broader range of GMSLR projections, also under different climate change scenarios. However, the results here already indicate that sea-level projections based on low-resolution climate models should be interpreted with great care, in particular, regarding estimates of the effects Antarctic basal melt.

MATERIAL AND METHODS

Model output

The standard model output of the CESM simulations consists of monthly averaged oceanic fields of sea surface height above geoid [i.e., dynamic sea level (*38*)], horizontal velocity, temperature, and salinity. For the atmospheric component of the CESM, we analyzed the (near surface) air temperature and (solid) precipitation. Besides, we retained the Antarctic sea-ice fractions from the sea-ice component of the CESM. The HR-CESM and the LR-CESM are spun up by 200 and 500 years, respectively. All the CESM simulations lasted for 101 years. Most of the monthly averaged quantities are converted to yearly averages unless stated otherwise. Two additional LR-CESM simulations (not used) were branched off after a spin-up period of 200 and 1200 years, the latter is used in (*21*). The shorter spin-up period has an initial sea-ice distribution similar to the HR-CESM control. The drawback of this simulation is that the (subsurface) ocean fields are strongly drifting, and the trends are sometimes in the same order of the applied forcing. The HR-CESM control that has a spin-up period of also 200 years does not show these strong drifts in the ocean fields. A longer spin-up period of the LR-CESM (1200 years) displays hardly any drift in the ocean fields. However, in this LR-CESM control simulation, the sea ice is further equilibrated and the maximum sea-ice extent dropped from 12.8 million to 14.5 million km^2 (model years 1200 to 1300). So, results from both additional simulations were not used here.

CMIP6 model output

We use results from the latest release of the CMIP6 and compare these to the output of our CESM simulations (Table 1). We analyzed the model output of the CMIP6 preindustrial control simulations and in which the atmospheric CO_2 levels increase each year by 1%. We analyze the monthly averaged oceanic temperature (variable "theato") fields and near surface air temperature (variable "tas") fields of the first 101 model years, as is done for the CESM output.

Reanalysis (Mercator)

We retained model output from the Operational Mercator global ocean physical reanalysis product (http://marine.copernicus.eu/services-portfolio/access-to-products/). The ocean component of Mercator (i.e., NEMO) has a horizontal resolution of 1/12°, 50 non-equidistant vertical levels, and covers the altimetry era (1993–2018). Mercator assimilates various observational datasets and the model is "steered" toward observations. We retained the monthly averaged temperature fields of the Mercator between 1993 and 2018.

Sea-ice observations

We obtained sea-ice measurements by the Scanning Multichannel Microwave Radiometer and Special Sensor Microwave Imager [http://nsidc.org/data/G02202, (*39*, *40*)]. We retained the monthly averaged sea-ice fraction fields from the NASA Team algorithm with Goddard Quality Check. The sea-ice fraction fields are analyzed between 1993 and 2018, same as for the reanalysis.

Contributions by steric effects

The local steric contribution (η_S) is determined from postprocessing the model output (*41*). The contribution of both thermal effects and haline effects is determined as the full-depth integral over the specific volume anomaly (*42*)

$$\eta_S = \int_{-H}^{0} \frac{\rho_0 - \rho(T,S,P)}{\rho_0}\, dz \quad (1)$$

The temperature, salinity, and pressure dependency are taken into account while determining the density, and $\rho_0 = 1028$ kg m^{-3}.

The steric contribution is expressed as an anomaly with respect to the initial value of the first model year. The globally averaged steric contribution, indicated by η_S^g, is shown in Fig. 1, also known as the global mean thermosteric sea-level rise (*38*). We corrected for any drift in η_S^g using the control simulations. After local ocean bottom pressure changes, the local thermosteric sea level eventually becomes η_S^g.

Contributions by glaciers

To determine the contribution to GMSLR by the melt of glaciers, we followed the procedure outlined in Church *et al.* (*34*). First, the 2-m GMST is determined for the HR-CESM and LR-CESM. Second, we determined the GMST anomaly with respect to the control simulations (see below for determining the anomalies). The time integral of the GMST anomaly between 2000 – t [indicated by $l(t)$] is used to determine the GMSLR contribution by glaciers

$$\eta_{\text{glaciers}}(t) = \text{fl}\,(t)^p \tag{2}$$

where f and p are constants, which are derived from four glacier models, and these values can be found in Church *et al.* (*34*) (their table 13.SM.2); negative values of $l(t)$ are set to zero. For the uncertainty in the projections at time t, we take 20% of $l(t)$ as the SD of a normal distribution. Third, we retained 2500 surrogate time series where a random number (independent of time) from the time dependent normal distribution is chosen. Last, we take the model mean over the four glaciers models, the percentile levels of η_{glaciers} are shown in fig. S3 (A and B).

Each of the 19 regions in the Randolph Glacier Inventory contribute to η_{glaciers}. Therefore, the contribution of each of the 19 regions to η_{glaciers} is scaled by its fraction of the global glacier volume. Here, we used the values in (*43*) of the modeled glacier volume in 2009 (their table 3), and we did not include the contribution of the glaciers in the Antarctic and sub-Antarctic region. The mass loss of each of the 19 glacier regions is multiplied by its fingerprint (due to GRD effects); the results are shown in fig. S3 (C and D). We used the 50% percentile level for η_{glaciers} in Fig. 1 and fig. S3 (C and D).

Contribution by the GrIS

Changes in the surface mass balance ($\Delta\text{SMB}_{\text{GrIS}}$) of the GrIS are governed by changes in snowfall and (surface) melt (*35*)

$$\Delta\text{SMB}_{\text{GrIS}} = \Delta\text{SF}_{\text{GrIS}} - 84.2\Delta T_{600}^{\text{JJA}} - 2.4\,(\Delta T_{600}^{\text{JJA}})^2 - 1.6\,(\Delta T_{600}^{\text{JJA}})^3 \tag{3}$$

where $\Delta\text{SF}_{\text{GrIS}}$ is the yearly snowfall anomaly over the GrIS and $\Delta T_{600}^{\text{JJA}}$ is the June to August temperature anomaly over the GrIS at 600 hPa. The anomalies are deviations from the control simulations (see below for determining the anomalies). The components of the surface mass balance are shown in fig. S4 (A and B). Negative values of $\Delta T_{600}^{\text{JJA}}$ are set to zero.

Ice dynamics and the positive melt-elevation feedback are not considered in relation (Eq. 3) because the GrIS topography is fixed (*35*). Following (*34*), the terms containing $\Delta T_{600}^{\text{JJA}}$ (melt terms) are multiplied by a factor E to adjust for the fixed GrIS topography. Here, E is a random chosen number from a uniform probability distribution in the range of 1.00 to 1.15 (time independent). Changes in $\Delta\text{SMB}_{\text{GrIS}}$ are converted to GMSLR (factor of 361.8 Gt mm^{-1}). The GMSLR by changes in the surface mass balance of the GrIS is shown in fig. S4 (C and D); here, we used 2500 surrogate time series for the percentile levels. The mass loss by the GrIS (using the 50% percentile) is multiplied by its fingerprint (due to GRD effects); the results are shown in Fig. 1 and fig. S4 (E and F).

Contribution by the AIS

Changes in the surface mass balance ($\Delta\text{SMB}_{\text{AIS}}$) of the AIS contribute to a negative GMSLR (*29*). We determined the snowfall anomaly (with respect to control simulation) over the AIS for the HR-CESM and LR-CESM. An increase in snowfall results in an increase in AIS dynamics (*34*) and the surface mass balance becomes

$$\Delta\text{SMB}_{\text{AIS}} = \sigma\Delta\text{SF}_{\text{AIS}} \tag{4}$$

where $\Delta\text{SF}_{\text{AIS}}$ is the snowfall anomaly over the AIS and σ is a random number chosen from a uniform probability distribution in the range of 0.65 to 1 (time independent). We converted the $\Delta\text{SMB}_{\text{AIS}}$ to GMSLR equivalent, and the 50% percentile from 2500 surrogates is shown in fig. S5 (blue curve).

Basal melt by increased oceanic temperatures on the continental shelfs surrounding Antarctica eventually leads to GMSLR (*7*). We followed the same procedure outlined in (*7*) and determined the vertically averaged temperature over the five Southern Ocean region (cf. Fig. 2A) for the CESM simulations (Fig. 2, B to F), and the vertical ranges for each region are provided in table 1 of Levermann *et al.* (*7*). Next, we determined the temperature anomaly (with respect to control simulation) for each region (indicated by ΔT_O; fig. S10, B to F), and the basal melt Δm is defined as

$$\Delta m(t) = \beta\Delta\, T_O(t) \tag{5}$$

where β is the melt sensitivity parameter varying uniformly between 7 and 16 m yr^{-1}°C^{-1} (time independent).

Using the appropriate response function [indicate by $R(t)$] for each Southern Ocean region, the basal melt can be converted to GMSLR

$$\Sigma(t) = \int_0^t m(t)\,R(t-\tau)\,\mathrm{d}\tau \tag{6}$$

The response functions are retained from 16 different ice-sheet models (*7*), and we used the last 101 years for each response function. For each ice-sheet model, we retained 2500 surrogates by varying β, and afterward, we determined the model mean of $\Sigma(t)$ for the 16 ice-sheet models. The GMSLR as a consequence of basal melt (i.e., 50% percentile) is shown in fig. S5 (red curve), and the contribution for each region is shown in Fig. 4.

The mass gain or loss by the AIS (using the 50% percentile) is multiplied by its fingerprint (due to GRD effects). For the increased snowfall anomaly, we used the fingerprint of the entire AIS. GMSLR as a result of basal melt at the East Antarctic region, half of the Ross region, and half of the Weddell region is multiplied by the fingerprint of East Antarctica. We included half of the GMSLR contribution of the Ross region and Weddell region since both regions consist of an eastern region and western region (*12*). The GMSLR contributions of the remaining regions (i.e., Amundsen region, Antarctic Peninsula, half of the Ross region, and half of the Weddell region) are multiplied by the fingerprint of West Antarctica. The final fingerprints of the AIS are shown in fig. S5 (C and D).

Dynamic sea-level changes

The sea surface height above geoid (variable "SSH") is part of the standard output of the CESM, referred to as the dynamic sea level

(*38*). The globally averaged dynamic sea level is about zero since the CESM has a volume constraint for the ocean and does not contribute to GMSLR; we uniformly removed the global mean from the dynamic sea-level fields. Local dynamic sea-level changes are shown in fig. S6 for the HR-CESM and LR-CESM.

Determining anomalies (e.g., of temperature)

The (depth-averaged) temperature anomalies are determined with respect to the control simulations. However, some of the temperature fields display a (significant) drift in the control simulations (fig. S2, A and B). First, we determined the linear trend (α_C) of a time series (y_C) in the control simulation. This linear trend was subtracted from the relevant time series ($\tilde{y} = y - \alpha_C$) and the control time series ($\tilde{y_C} = y_C - \alpha_C$). Next, the time mean of the detrended control simulation ($\bar{y_C}$) was subtracted to retain the anomalies ($y' = \tilde{y} - \bar{y_C}$). This procedure was applied to all temperature time series, as well as for the snowfall time series.

Area-weighted correlation coefficient and RMS deviation

First, we determined the area-weighted temperature between 80°S and 60°S of two climate models, indicated by $\bar{T}^1$ and $\bar{T}^2$. Next, the area-weighted covariance is determined using the following expression

$$\mathrm{cov}(T^1, T^2) = \sum_i A_i (T_i^1 - \bar{T}^1)(T_i^2 - \bar{T}^2) \tag{7}$$

where A_i is the normalized area of a grid cell i with respect to the total area A. The area-weighted correlation coefficient, r, becomes

$$r = \frac{\mathrm{cov}(T^1, T^2)}{\sqrt{\mathrm{cov}(T^1, T^1)\,\mathrm{cov}(T^2, T^2)}} \tag{8}$$

In a similar way, the area-weighted RMS deviation can be determined using

$$\mathrm{RMS} = \sqrt{\sum_i A_i (T_i^1 - T_i^2)^2} \tag{9}$$

For the HR-CESM and LR-CESM, we interpolated the temperature fields onto the Mercator grid and the CMIP6 native grids before determining r and RMS.

Barotropic streamfunction

The barotropic flow is defined as the full-depth integral of the horizontal velocity

$$\overrightarrow{\mathbf{BF}} = \int_{-H}^{0} \vec{\mathbf{v}}\, \mathrm{d}z \tag{10}$$

Starting from Antarctica (with a value of 0 for the BSF), we integrate the zonal component of the barotropic flow (indicated by BF_x) meridionally to determine the BSF

$$\mathrm{BSF}(x, y, t) = \int_{90^\circ\mathrm{S}}^{y} \mathrm{BF}_x(x, y', t)\, \mathrm{d}y' \tag{11}$$

For convenience, the average value of the BSF along the African coast line is subtracted from the entire BSF field.

SUPPLEMENTARY MATERIALS

Supplementary material for this article is available at http://advances.sciencemag.org/cgi/content/full/7/15/eabf1674/DC1

REFERENCES AND NOTES

1. X. Chen, X. Zhang, J. A. Church, C. S. Watson, M. A. King, D. Monselesan, B. Legresy, C. Harig, The increasing rate of global mean sea-level rise during 1993–2014. *Nat. Clim. Chang.* **7**, 492–495 (2017).
2. C. S. Watson, N. J. White, J. A. Church, M. A. King, R. J. Burgette, B. Legresy, Unabated global mean sea-level rise over the satellite altimeter era. *Nat. Clim. Chang.* **5**, 565–568 (2015).
3. M. Ablain, B. Meyssignac, L. Zawadzki, R. Jugier, A. Ribes, G. Spada, J. Benvenitse, A. Cazenave, N. Picot, Uncertainty in satellite estimates of global mean sea-level changes, trend and acceleration. *Earth Syst. Sci. Data* **11**, 1189–1202 (2019).
4. J. Hinkel, J. A. Church, J. M. Gregory, E. Lambert, G. Le Cozannet, J. Lowe, K. L. McInnes, R. J. Nicholls, T. D. van der Pol, R. van de Wal, Meeting user needs for sea level rise information: A decision analysis perspective. *Earth's Future* **7**, 320–337 (2019).
5. R. J. Nicholls, A. Cazenave, Sea-level rise and its impact on coastal zones. *Science* **328**, 1517–1520 (2010).
6. T. F. Stocker, D. Qin, G.-K. Plattner, M. Tignor, S. K. Allen, J. Boschung, A. Nauels, Y. Xia, V. Bex, P. M. Midgley, *Climate Change 2013: The Physical Science Basis. Contribution of Working Group I to the Fifth Assessment Report of the Intergovernmental Panel on Climate Change* (Cambridge Univ. Pres, 2013), pp. 1535.
7. A. Levermann, R. Winkelmann, T. Albrecht, H. Goelzer, N. R. Golledge, R. Greve, P. Huybrechts, J. Jordan, G. Leguy, D. Martin, M. Morlighem, F. Pattyn, D. Pollard, A. Quiquet, C. Rodehacke, H. Seroussi, J. Sutter, T. Zhang, J. van Breedam, R. Calov, R. DeConto, C. Dumas, J. Garbe, G. H. Gudmundsson, M. J. Hoffman, A. Humbert, T. Kleiner, W. H. Lipscomb, M. Meinshausen, E. Ng, S. M. J. Nowicki, M. Perego, S. F. Price, F. Saito, N. J. Schlegel, S. Sun, R. S. W. van de Wal, Projecting Antarctica's contribution to future sea level rise from basal ice shelf melt using linear response functions of 16 ice sheet models (LARMIP-2). *Earth Syst. Dynam.* **11**, 35–76 (2020).
8. J. A. Church, P. U. Clark, A. Cazenave, J. M. Gregory, S. Jevrejeva, A. Levermann, M. A. Merrifield, G. A. Milne, R. S. Nerem, P. D. Nunn, A. J. Payne, W. T. Pfeffer, D. Stammer, A. S. Unnikrishnan, *Chapter 13: Sea Level Change* (The Intergovernmental Panel on Climate Change, 2013).
9. E. Rignot, J. L. Bamber, M. R. van den Broeke, C. Davis, Y. Li, W. J. van de Berg, E. van Meijgaard, Recent Antarctic ice mass loss from radar interferometry and regional climate modelling. *Nat. Geosci.* **1**, 106–110 (2008).
10. J. L. Bamber, R. E. Riva, B. L. Vermeersen, A. M. LeBrocq, Reassessment of the potential sea-level rise from a collapse of the West Antarctic Ice Sheet. *Science* **324**, 901–903 (2009).
11. The IMBIE Team, Mass balance of the Antarctic Ice Sheet from 1992 to 2017. *Nature* **558**, 219–222 (2018).
12. E. Rignot, J. Mouginota, B. Scheuchl, M. van den Broeke, M. J. van Wessem, M. Morlighem, Four decades of Antarctic ice sheet mass balance from 1979–2017. *Proc. Natl. Acad. Sci. U.S.A.* **116**, 1095–1103 (2019).
13. T. L. Frölicher, J. L. Sarmiento, D. J. Paynter, J. P. Dunne, J. P. Krasting, M. Winton, Dominance of the Southern Ocean in anthropogenic carbon and heat uptake in CMIP5 models. *J. Climate* **28**, 862–886 (2015).
14. J.-B. Sallée, Southern ocean warming. *Oceanography* **31**, 52–62 (2018).
15. J. L. Russell, R. J. Stouffer, K. W. Dixon, Intercomparison of the Southern Ocean circulations in IPCC coupled model control simulations. *J. Climate* **19**, 4560–4575 (2006).
16. K. E. Trenberth, J. T. Fasullo, Simulation of present-day and twenty-first-century energy budgets of the southern oceans. *J. Climate* **23**, 440–454 (2010).
17. R. J. Small, J. Bacmeister, D. Bailey, A. Baker, S. Bishop, F. Bryan, J. Caron, J. Dennis, P. Gent, H.-m. Hsu, M. Jochum, D. Lawrence, E. Muñoz, P. diNezio, T. Scheitlin, R. Tomas, J. Tribbia, Y.-h. Tseng, M. Vertenstein, A new synoptic scale resolving global climate simulation using the Community Earth System Model. *J. Adv. Model. Earth Syst.* **6**, 1065–1094 (2014).
18. S.-E. Brunnabend, H. A. Dijkstra, M. A. Kliphuis, B. van Werkhoven, H. E. Bal, F. Seinstra, J. Maassen, M. van Meersbergen, Changes in extreme regional sea surface height due to an abrupt weakening of the Atlantic meridional overturning circulation. *Ocean Sci.* **10**, 881–891 (2014).
19. D. V. Sein, N. V. Koldunov, S. Danilov, Q. Wang, D. Sidorenko, I. Fast, T. Rackow, W. Cabos, T. Jung, Ocean modeling on a mesh with resolution following the local Rossby radius. *J. Adv. Model. Earth Syst.* **9**, 2601–2614 (2017).
20. D. Sidorenko, H. F. Goessling, N. V. Koldunov, P. Scholz, S. Danilov, D. Barbi, W. Cabos, O. Gurses, S. Harig, C. Hinrichs, S. Juricke, G. Lohmann, M. Losch, L. Mu, T. Rackow, N. Rakowsky, D. Sein, T. Semmler, X. Shi, C. Stepanek, J. Streffing, Q. Wang, C. Wekerle, H. Yang, T. Jung, Evaluation of FESOM2. 0 Coupled to ECHAM6. 3: Preindustrial and HighResMIP simulations. *J. Adv. Model. Earth Syst.* **11**, 3794–3815 (2019).
21. R. M. van Westen, H. A. Dijkstra, C. G. van der Boog, C. A. Katsman, R. K. James, T. J. Bouma, O. Kleptsova, R. Klees, R. E. M. Riva, D. C. Slobbe, M. Zijlema, J. D. Pietrzak, Ocean model resolution dependence of Caribbean sea-level projections. *Sci. Rep.* **10**, 14599 (2020).
22. R. Hallberg, Using a resolution function to regulate parameterizations of oceanic mesoscale eddy effects. *Ocean Model.* **72**, 92–103 (2013).

23. R. M. van Westen, H. A. Dijkstra, Multidecadal preconditioning of the Maud Rise polynya region. *Ocean Sci.* **16**, 1443–1457 (2020).
24. D. Le Bars, J. P. Viebahn, H. A. Dijkstra, A Southern Ocean mode of multidecadal variability. *Geophys. Res. Lett.* **43**, 2102–2110 (2016).
25. T. Frederikse, F. W. Landerer, L. Caron, The imprints of contemporary mass redistribution on local sea level and vertical land motion observations. *Solid Earth* **10**, 1971–1987 (2019).
26. D. A. Smeed, S. A. Josey, C. Beaulieu, W. E. Johns, B. I. Moat, E. Frajka-Williams, D. Rayner, C. S. Meinen, M. O. Baringer, H. L. Bryden, G. D. McCarthy, The North Atlantic Ocean is in a state of reduced overturning. *Geophys. Res. Lett.* **45**, 1527–1533 (2018).
27. L. Caesar, S. Rahmstorf, A. Robinson, G. Feulner, V. Saba, Observed fingerprint of a weakening Atlantic Ocean overturning circulation. *Nature* **556**, 191–196 (2018).
28. L. M. Beal, W. P. De Ruijter, A. Biastoch, R. Zahn; SCOR/WCRP/IAPSO Working Group 136, On the role of the Agulhas system in ocean circulation and climate. *Nature* **472**, 429–436 (2011).
29. J. Gregory, P. Huybrechts, Ice-sheet contributions to future sea-level change. *Philos. Trans. R. Soc. A* **364**, 1709–1732 (2006).
30. Y. Nakayama, G. Manucharyan, H. Zhang, P. Dutrieux, H. S. Torres, P. Klein, H. Seroussi, M. Schodlok, E. Rignot, D. Menemenlis, Pathways of ocean heat towards pine island and thwaites grounding lines. *Sci. Rep.* **9**, 16649 (2019).
31. S. A. Cunningham, S. G. Alderson, B. A. King, M. A. Brandon, Transport and variability of the Antarctic circumpolar current in drake passage. *J. Geophys. Res. Oceans* **108**, 8084 (2003).
32. M. P. Meredith, P. L. Woodworth, T. K. Chereskin, D. P. Marshall, L. C. Allison, G. R. Bigg, K. Donohue, K. J. Heywood, C. W. Hughes, A. Hibbert, A. M. Hogg, H. L. Johnson, L. Jullion, B. A. King, H. Leach, Y.-D. Lenn, M. A. M. Maqueda, D. R. Munday, A. C. Naveira Garabato, C. Provost, J.-B. Sallée, J. Sprintall, Sustained monitoring of the Southern Ocean at Drake Passage: Past achievements and future priorities. *Rev. Geophys.* **49**, RG4005 (2011).
33. A. L. Stewart, A. M. Hogg, Reshaping the Antarctic circumpolar current via Antarctic bottom water export. *J. Phys. Oceanogr.* **47**, 2577–2601 (2017).
34. J. A. Church, P. U. Clark, A. Cazenave, J. M. Gregory, S. Jevrejeva, A. Levermann, M. A. Merrifield, G. A. Milne, R. S. Nerem, P. D. Nunn, A. J. Payne, W. T. Pfeffer, D. Stammer. A. S. Unnikrishnan, *Chapter 13: Sea Level Change Supplementary Material* (The Intergovernmental Panel on Climate Change, 2013).
35. X. Fettweis, B. Franco, M. Tedesco, J. H. van Angelen, J. T. M. Lenaerts, M. R. van den Broeke, H. Gallée, Estimating the Greenland ice sheet surface mass balance contribution to future sea level rise using the regional atmospheric climate model MAR. *Cryosphere* **7**, 469–489 (2013).
36. W. Weijer, M. E. Maltrud, M. W. Hecht, H. A. Dijkstra, M. A. Kliphuis, Response of the Atlantic Ocean circulation to Greenland Ice Sheet melting in a strongly-eddying ocean model. *Geophys. Res. Lett.* **39**, L09606 (2012).
37. S.-E. Brunnabend, H. A. Dijkstra, M. A. Kliphuis, H. E. Bal, F. Seinstra, B. van Werkhoven, J. Maassen, M. van Meersbergen, Changes in extreme regional sea level under global warming. *Ocean Sci.* **13**, 47–60 (2017).
38. J. M. Gregory, S. M. Griffies, C. W. Hughes, J. A. Lowe, J. A. Church, I. Fukimori, N. Gomez, R. E. Kopp, F. Landerer, G. Le Cozannet, R. M. Ponte, D. Stammer, M. E. Tamisiea, R. S. W. van de Wal, Concepts and terminology for sea level: Mean, variability and change, both local and global. *Surv. Geophys.* **40**, 1251–1289 (2019).
39. G. Peng, W. Meier, D. Scott, M. Savoie, A long-term and reproducible passive microwave sea ice concentration data record for climate studies and monitoring. *Earth Syst. Sci. Data* **5**, 311–318 (2013).
40. W. Meier, F. Fetterer, M. Savoie, S. Mallory, R. Duerr, J. Stroeve, *NOAA/NSIDC Climate Data Record of Passive Microwave Sea Ice Concentration, Version 3* (National Snow and Ice Data Center, Boulder, CO, 2019); https://nsidc.org/data/g02202/versions/3.
41. R. J. Greatbatch, A note on the representation of steric sea level in models that conserve volume rather than mass. *J. Geophys. Res.* **99**, 12767–12771 (1994).
42. K. Richter, R. Riva, H. Drange, Impact of self-attraction and loading effects induced by shelf mass loading on projected regional sea level rise. *Geophys. Res. Lett.* **40**, 1144–1148 (2013).
43. B. Marzeion, A. Jarosch, M. Hofer, Past and future sea-level change from the surface mass balance of glaciers. *Cryosphere* **6**, 1295–1322 (2012).
44. B. D. Santer, T. M. L. Wigley, J. S. Boyle, D. J. Gaffen, J. J. Hnilo, D. Nychka, D. E. Parker, K. E. Taylor, Statistical significance of trends and trend differences in layer-average atmospheric temperature time series. *J. Geophys. Res. Atmos* **105**, 7337–7356 (2000).

Acknowledgments: We thank M. Kliphuis (IMAU, UU) for the assistance with the CESM simulations. All computations were performed on the Cartesius at SURFsara in Amsterdam within project 17239. We thank E. Lambert (KNMI) for the useful discussions on the Greenland and AIS contributions to global mean sea-level rise. The spatial patterns for the GRD effects (fingerprints) were provided by T. Frederikse. **Author contributions:** R.M.v.W. and H.A.D. conceived the idea for this study and wrote the main manuscript text. R.M.v.W. conducted the analysis and prepared all figures. **Competing interests:** The authors declare that they have no competing interests. **Data and materials availability:** The CMIP6 model output is provided by the World Climate Research Programme's Working Group on Coupled Modeling. The Mercator reanalysis product can be accessed at http://marine.copernicus.eu/services-portfolio/access-to-products/. The sea-ice products can be accessed at http://nsidc.org/data/G02202. The data from the CESM simulations used in this work are available upon reasonable request from the authors. Processed CESM and CMIP6 model output and part of the analysis scripts (Python 2.7.9) can be accessed at https://github.com/RenevanWesten/SA-Eddies_GMSLR. The maps are generated using the BASEMAP package in Python.

Submitted 8 October 2020
Accepted 22 February 2021
Published 9 April 2021
10.1126/sciadv.abf1674

Citation: R. M. van Westen, H. A. Dijkstra, Ocean eddies strongly affect global mean sea-level projections. *Sci. Adv.* **7**, eabf1674 (2021).

Science Advances

Ocean eddies strongly affect global mean sea-level projections

René M. van Westen and Henk A. Dijkstra

Sci Adv **7** (15), eabf1674.
DOI: 10.1126/sciadv.abf1674